

PAPER

Light-activated piezoelectric linear motor by using a serial bimorph made of an optopiezoelectric composite

To cite this article: Tsun-Hsu Chen *et al* 2018 *Smart Mater. Struct.* **27** 105050

View the [article online](#) for updates and enhancements.

Light-activated piezoelectric linear motor by using a serial bimorph made of an optopiezoelectric composite

Tsun-Hsu Chen¹, Tsung-Yu Chu¹, Yu-Min Lin¹, Shih-Jue Lin²,
Jen-Tau Gu² and Yu-Hsiang Hsu¹ 

¹Institute of Applied Mechanics, National Taiwan University, No. 1, Sec.4, Roosevelt Rd., Taipei, Taiwan 106, Republic of China

²Green Rich Technology Co., Ltd No. 31, Keyi St., Chunan, Miaoli 350, Taiwan, Republic of China

E-mail: yhhsu@iam.ntu.edu.tw

Received 7 March 2018, revised 14 August 2018

Accepted for publication 22 August 2018

Published 21 September 2018



CrossMark

Abstract

In this paper, we report a new method to activate and control a piezoelectric linear motor using a switching light source through two transparent electrodes and a photoconductive coating. This coating is composed of titanium oxide phthalocyanine (TiOPc), electron transport materials, hole transport materials, and polyvinyl butyral binder. It is used to replace one of the surface electrodes of a piezoelectric serial bimorph to provide an optical interface and to construct an optopiezoelectric composite. The weight percentage of TiOPc nanoparticles, solvent compositions, and film thickness are studied to identify the optimal coating to match the electrical impedance of the piezoelectric serial bimorph in both on and off states. Experimental results show that the photoconductive coating has a good on–off ratio and low electrical impedance under conditions of high concentration of TiOPc, small film thickness, high light intensity, and low frequency. To design this motor based on a one-frequency-two-mode driving method, an analytical solution is derived and an optopiezoelectric linear motor (OP-LM) is developed. Our analytical analysis, finite element simulation, and experimental results demonstrate that traveling waves can be generated by driving this motor at a frequency between the first and the second bending modes with a 90° phase difference between two designed actuating areas. The optimal condition is to match the driving frequency and light switching frequency. The moving direction and velocity of objects in different weight can be optically controlled by illuminating different areas of an optopiezoelectric motor with two 10 W power LEDs and masks. Discussions on the developed theory, simulation, and experimental studies of the OP-LM are provided in this paper.

Supplementary material for this article is available [online](#)

Keywords: optopiezoelectric composite, optopiezoelectric linear motor, linear piezoelectric motor, titanyl phthalocyanine, photoconductive coating, two-mode excitation

(Some figures may appear in colour only in the online journal)

1. Introduction

In recent years, the concept of using a photoconductive coating to provide an optical interface for manipulating particles, cells, and droplets in a lab-on-a-chip system has been reported. It has enabled one to control multiple components

with complex functions optically. It offers an optical interface to create different patterns of activation area dynamically to perform complex tasks on a chip. For example, photoconductive hydrogenated amorphous silicon (α -Si:H) has been applied to an optoelectronic tweezer [1–3]. Photoconductive α -Si:H and a transparent electrode have been used

to replace one of the electrodes of a dielectrophoretic microfluidic device. By selectively illuminating the photoconductive α -Si:H layer to reduce resistivity, a patterned electrical field can be generated and light induced dielectrophoresis (LIDEP) can be created. Micron-sized particles and cells can be trapped, moved, and positioned in a microfluidic channel. Similar concepts and methods have been applied to the electrowetting-on-dielectric (EWOD) method for droplet manipulation [4]. Surface energy of the exposed area can be adjusted to move droplets. Nevertheless, a vacuum deposition system, such as plasma-enhanced chemical vapor deposition, often is needed to produce a high quality photoconductive α -Si:H coating. The processing temperature can be as high as 300 °C, and the deposited film is fragile. The requirement of process compatibility is very strict, and its application for flexible substrates is limited.

Titanly phthalocyanine (TiOPc) is another organic photoconductive material that has been used for both LIDEP [5, 6] and EWOD [7, 8]. The photoreceptor layers used in these applications usually are based on the composition developed for photoreceptor drums. A standard spin coating technique is used to create TiOPc photoconductive layer on the lab-on-a-chip device. The requirement of process compatibility is much easier than α -Si:H. In these applications, the weight percentage of TiOPc usually is low and its electrical impedance before and after light exposure can be considerably high. For a 9.1% (w/w) α -TiOPc dispersed in a polycarbonate (PC) resin, we found that the resistivity could be as high as $\sim 10^{11}$ and $\sim 10^{13}$ Ω cm in conditions with and without light exposure, respectively. This provides a good impedance match on LIDEP and EWOD applications since their electrical impedance also has a high value. In addition, TiOPc photoconductive coating provides excellent flexibility due to its polymer-based resin. Taking these superior characteristics, we previously reported on creating a microfluidic pump based on an optopiezoelectric composite composed of a TiOPc photoconductive layer and a piezoelectric PVDF (polyvinylidene fluoride) polymer [9]. Using a high concentration of TiOPc, two separated micropumps could be activated optically. This study demonstrated that the optopiezoelectric composite could serve as the actuator to optically drive a microfluidic pump at 1 Hz. The response of the optopiezoelectric composite provides good impedance matching on both before and after light illumination under DC and low frequency region.

Following this line of thinking, we present our study on applying a ceramic-based optopiezoelectric composite to a piezoelectric linear motor here. We verified that, using an optopiezoelectric composite to be its core, the motor can be activated and controlled optically. The linear piezoelectric motor has drawn considerable attention since its structure is simple and it can be fabricated easily. Due to its finite boundaries, however, the reflected waves from the boundaries can generate resonant modes easily and hinder the generation of a continuous and stable traveling wave. Methods have been proposed to build linear traveling wave motors using piezoelectric actuators. For example, Kuribayashi, *et al* developed the first piezoelectric linear motor in 1985 using one actuator

and one absorber [10]. The first piezoelectric actuator was used to generate the traveling wave, and the second piezoelectric absorber was connected to an RL passive circuit to sink energy of the propagated mechanical energy. This method was able to eliminate the reflected waves from the finite boundary. In 1989, Takano and Tomikawa reported another method by combining the first longitudinal mode and the forth-bending mode [11]. In this way, multiple elliptic waves can be generated on a linear finite structure, and it could be used to serve as a linear motor. In the same year, Tomikawa *et al* reported another method named two-mode excitation that can generate traveling waves on a 1D finite structure by using two sets of piezoelectric actuators [12]. The driving frequency was chosen between two adjacent bending modes with a 90° out of phase difference. This approach was further studied by Hariri, *et al* in recent years with two piezoelectric patches [13]. The second report of Hariri, *et al* also demonstrated that the position of these two piezoelectric actuators can affect the performance of generated traveling waves [14]. Applying the concept of two-mode excitation, Loh and Ro used two bolted Langevin-type transducers to apply 90° out of phase excitations to generate traveling waves on a long 1D structure [15]. Optimizing process of this approach to improve the quality of generated traveling waves was also reported by Dehez *et al* [16].

In this study, we derived an analytical theory to show how the traveling wave could be induced using a single frequency to excite two adjacent bending modes through two piezoelectric actuators. We further demonstrated that the key to control the direction and velocity of induced traveling waves was determined by the location and size of the two piezoelectric actuators. This method was named one-frequency-two-mode (OFTM) in this paper for simplicity. We applied the concept of optopiezoelectric composite to develop an optopiezoelectric linear motor (OP-LM) using a piezoelectric serial bimorph. We verified that this linear motor could be optically activated and controlled. To match the electromechanical performance of the piezoelectric serial bimorph at higher frequency range than [10], we performed a series studies on the TiOPc based photoconductive coating with different combinations of Y-TiOPc nanoparticles (NPs) and solvent compositions. A preliminary study on the composition of TiOPc NPs was reported previously in a conference paper [17]. In this paper, we report a complete study and further demonstrate that the on-off ratio of the photoconductive coating could be adjusted by controlling the solid content of the TiOPc NPs, solvent composition, and coating thickness. This could be used to match the electrical impedance of the piezoelectric serial bimorph for both on and off states. Based on the developed photoconductive coating and analytical theory, we developed an OP-LM that can be optically controlled. We further demonstrated that the direction of traveling waves can be controlled optically. This design enable the capability to change the performance of the motor by spatially defined actuators. It eliminated the limitation of reported piezoelectric linear motors that their performance is determined once the location and size of piezoelectric actuators were chosen. Detailed discussions on the analytical

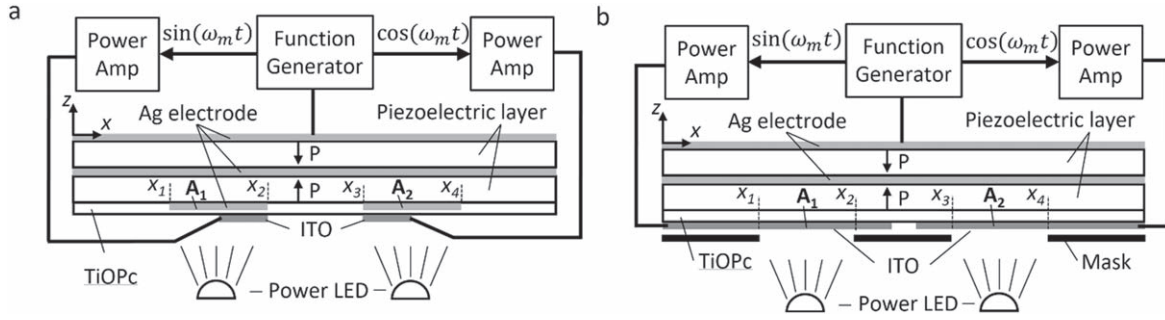


Figure 1. Design and experimental setup of two optopiezoelectric linear motors, where the impedance match between the photoconductive coating and actuating areas is achieved by using ITO electrodes (a) or a mask (b).

analysis, finite element simulation, and experimental study of the OP-LM are presented in this paper.

2. Design of the OFTM OP-LM

Figures 1(a) and (b) show two types of the OFTM OP-LM developed in this study. Instead of attaching piezoelectric sheets onto a 1D elastic plate, as suggested in [12–14], we used a 1D piezoelectric serial bimorph to serve as the core structure of the OP-LM. The two OFTM actuators can be created by designing the location and size of surface electrodes on one side of the serial bimorph, which are indicated by A_1 and A_2 in figures 1(a) and (b). These two actuating areas are defined by edges of two remaining Ag electrodes (figure 1(a)) or light-activated regions (figure 1(b)) at x_1 , x_2 , x_3 , and x_4 . Furthermore, using a bimorph structure, the actuating performance of the bending mode can be optimized. Lead zirconate titanate (PZT) piezoelectric ceramic was chosen as the piezoelectric material in this study. It is a commercialized piezoelectric ceramic, and the fabrication process of a serial bimorph is well-developed. Because we needed to match electrical impedance of the photoconductive coating and the piezoelectric bimorph during both on and off states, light-illuminating areas and the resultant actuating areas were considered together. Since the electrical impedance of the photoconductive coating in lateral direction was several orders higher than the one in thickness direction, we designed two different types of the OP-LM based on this characteristic to match two types of power LEDs with different illuminating spectrums. Figure 1(a) shows the first design. It used two Ag electrodes to define the two actuating areas, and the photoconductive coating was coated on top of these electrodes followed by sputtering two designed ITO transparent electrodes. These two ITO electrodes were used to define the conductive region for matching the electrical impedance of the actuating area and the photoconductive layer. Thus, a mask was not needed and the photoconductive coating can be activated entirely. The second method was to completely replace one of Ag electrodes with the photoconductive coating and two ITO electrodes with a small separation (figure 1(b)). The direction and driving force of the traveling waves can be controlled by using different masks for activating different locations and areas of the OP-LM. The

impedance matching was determined by the activating area. Finally, these two actuating areas were driven by 90° out of phase signals through two power amplifiers to generate traveling waves on these two OP-LMs.

The x - y - z axes of the 1D plate are aligned with the 1-, 2-, 3-axes of two PZT layers. Thus, the transverse isotropic property of the PZT can be applied in the analytical analysis. According to the theory for piezoelectric laminates and assuming that the internal damping effect is negligible [18, 19], the governing equation of a serial piezoelectric bimorph with two separate rectangular actuating areas can be expressed as:

$$D_{11} \frac{\partial^4 w}{\partial x^4} + \rho h \frac{\partial^2 w}{\partial t^2} = -\frac{\partial^2}{\partial x^2} \left\{ \sum_{n=1}^2 P_n z V_1(t) [e_{31}(x)]_1 + \sum_{n=1}^2 P_n z V_2(t) [e_{31}(x)]_2 \right\}, \quad (1)$$

where D_{11} , ρ , h represent the flexural rigidity, density, and the thickness of the bimorph plate, and the width of the piezoelectric bimorph is set to be 1. The deflection of the bimorph plate is $w = w(x, t)$. P_n and its subscript n represent the poling direction and the top and bottom layers of the piezoelectric bimorph, where P_1 and P_2 equal to 1 and -1 , respectively. z is the distance of the neutral plane of the bimorph to the central plane of each piezoelectric layer. As the photoconductive coating is polymer based, its elasticity is more than 30 times softer than PZT. Furthermore, its thickness is 20 times thinner than the piezoelectric bimorph. Thus, the neutral plan of the OP-LM can be considered to be at the interface of the two piezoelectric layers of the bimorph structure. The locations and areas of the two rectangular actuating regions are represented by $[e_{31}(x)]_1$ and $[e_{31}(x)]_2$ in equation (1), where e_{31} is the piezoelectric stress constant and the width is set to be 1. Then, they can be expressed via Heaviside function $H(x)$ as:

$$[e_{31}(x)]_1 = e_{31}[H(x - x_1) - H(x - x_2)] \quad (2a)$$

and

$$[e_{31}(x)]_2 = e_{31}[H(x - x_3) - H(x - x_4)]. \quad (2b)$$

Finally, $V_1(t)$ and $V_2(t)$ represent the driving voltage and its temporal phase information of the two actuators. The suggested driving frequency (ω_m) of the OFTM linear motor was between two adjacent resonant modes, and the driving

frequency at the middle of the two resonant frequency was experimentally verified. It was demonstrated that drove two actuators at a 90° phase difference can induce traveling waves on a 1D finite structure [13, 14]. In this study, the first and the second bending modes were chosen, and ω_m was set between ω_1 and ω_2 . The first and the second bending modes were chosen was to match the electrical impedance of the photoconductive coating. Note that the following analytical analysis can further extend to higher bending modes. Our analytical analysis shows that the location and size of the two actuating areas determine the direction and amplitude of induced traveling waves.

The driving voltages $V_1(t)$ and $V_2(t)$ in equation (1) can be written as:

$$V_1 = V \sin(\omega_m t) \quad (3a)$$

and

$$V_2 = V \cos(\omega_m t), \quad (3b)$$

where V is the amplitude of the driving voltage and the subscripts 1 and 2 represent it being for actuator \mathbf{A}_1 or \mathbf{A}_2 . Substituting equations (2a), (2b) and (3a), (3b) into equation (1), the governing equation is simplified to

$$D_{11} \frac{\partial^4 w}{\partial x^4} + \rho h \frac{\partial^2 w}{\partial t^2} = -2he_{31}V \{[\delta'(x - x_1) - \delta'(x - x_2)]\sin(\omega_m t) + [\delta'(x - x_1) - \delta'(x - x_2)]\cos(\omega_m t)\}, \quad (4)$$

where δ is the Dirac delta function and the double amount of moment generated by the bimorph structure is expressed by multiplying 2 to the driving term on the right-hand side of equation (4). Since the structure of the OP-LM is a fixed-fixed 1D plate, the boundary conditions of fixed ends on two sides are $\Phi_i(0) = 0$, $\Phi'_i(0) = 0$, $\Phi_i(L) = 0$, and $\Phi'_i(L) = 0$, where L is the total length of the piezoelectric bimorph. The displacement field $w(x, t)$ can be expressed by the superposition of the eigenfunctions $\Phi_i(x)$:

$$w(x, t) = \sum_{i=1}^{\infty} \Phi_i(x) T_i(t), \quad (5)$$

where $T_i(t)$ represent the amplitude of the i th mode. $\Phi_i(x)$ can be solved via eigenfunction expansions and substituting boundary conditions of two fixed ends, and its general form is

$$\Phi_i(x) = \cosh(\lambda_i x) - \cos(\lambda_i x) - \alpha_i [\sinh(\lambda_i x) - \sin(\lambda_i x)], \quad (6)$$

where

$$\alpha_i = [\cosh(\lambda_i L) - \cos(\lambda_i L)] / [\sinh(\lambda_i L) - \sin(\lambda_i L)], \quad (7)$$

and

$$\cosh(\lambda_i L) \times \cos(\lambda_i L) = 1, \quad (8)$$

and λ_i is the characteristic wavelength of the i th mode. Taking a full field integration of equation (4) with respect to the j th mode, this partial differential equation can be decomposed into multiple ordinary differential equations (ODEs), where

the j th ODE becomes

$$\frac{d^2 T_j(t)}{dt^2} + \omega_j^2 T_j(t) = \frac{2Ve_{31}}{\rho K_j} \{[\Phi'_j(x_1) - \Phi'_j(x_2)] \times \sin(\omega_j t) + [\Phi'_j(x_3) - \Phi'_j(x_4)] \cos(\omega_j t)\}, \quad (9)$$

and

$$K_j = \int_0^L \Phi_j^2(x) dx, \quad (10)$$

The resonant frequency of the j th mode is represented by ω_j , and it can be correlated with λ_i by the following dispersion relationship

$$\lambda_j^4 = \frac{\rho h}{EI} \omega_j^2. \quad (11)$$

Let the driving frequency to be ω_m , and use initial conditions of $T_j(0) = 0$ and $T'_j(0) = 0$. Then, applying standard Laplace and inverse-Laplace transforms, $T_j(t)$ can be written as:

$$T_j(t) = \frac{Ve_{31}}{\rho \omega_j K_j} \{[\Phi'_j(x_1) - \Phi'_j(x_2)] F_L(\omega_m t) + [\Phi'_j(x_3) - \Phi'_j(x_4)] F_R(\omega_m t)\}, \quad (12)$$

where

$$F_L(\omega_m t) = \frac{1}{\omega_m + \omega_j} [\sin(\omega_m t) + \sin(\omega_j t)] - \frac{1}{\omega_m - \omega_j} [\sin(\omega_m t) - \sin(\omega_j t)] \quad (13a)$$

and

$$F_R(\omega_m t) = \frac{1}{\omega_m + \omega_j} [\cos(\omega_m t) - \cos(\omega_j t)] - \frac{1}{\omega_m - \omega_j} [\cos(\omega_m t) - \cos(\omega_j t)] \quad (13b)$$

represent the time domain contribution of actuators at areas \mathbf{A}_1 and \mathbf{A}_2 , respectively. Thus, the general solution of equation (5) for a fixed-fixed OP-LM is derived. Since the driving principle of OFTM is that the two bending modes next to the driving frequency are excited the most and dominate, the first (ω_1) and the second resonant modes (ω_2) can both be excited by the single driving frequency (ω_m) between them. Thus, a traveling wave can be generated on the OP-LM. Following this concept, we can derive the induced traveling waves by solving the superposition of the first and the second bending modes. The induced vibration can be written as:

$$w = w_m + w_r = \sum_{j=1}^2 \{\Phi_j(x) [A_j \sin(\omega_m t) + B_j \cos(\omega_m t)]\} + \sum_{j=1}^2 \{-\Phi_j(x) [C_j \sin(\omega_j t) + D_j \cos(\omega_j t)]\}, \quad (14)$$

where

$$A_j = P_j [\Phi'_j(x_1) - \Phi'_j(x_2)] F(\omega_m, \omega_j) \text{ with } j = 1 \text{ or } 2, \quad (15a)$$

$$B_j = P_j [\Phi'_j(x_3) - \Phi'_j(x_4)] F(\omega_m, \omega_j) \text{ with } j = 1 \text{ or } 2, \quad (15b)$$

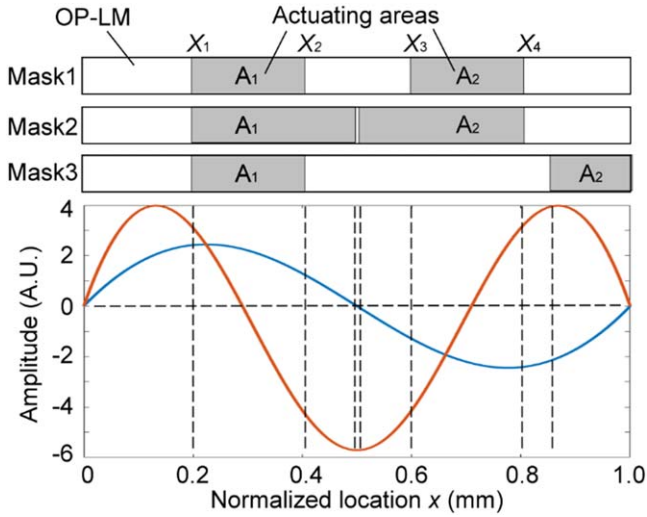


Figure 2. Illustrations of three different designs of two actuating areas (A_1 and A_2) for the OP-LM. Their corresponding locations on bending angle profiles of the first $\Phi'_1(x)$ (blue line) and the second $\Phi'_2(x)$ (red line) modes are indicated with dashed lines.

$$C_j = P_j[\Phi'_j(x_1) - \Phi'_j(x_2)]F(\omega_m, \omega_j) \text{ with } j = 1 \text{ or } 2, \quad (15c)$$

$$D_j = P_j[\Phi'_j(x_3) - \Phi'_j(x_4)]F(\omega_m, \omega_j) \text{ with } j = 1 \text{ or } 2, \quad (15d)$$

and $P_j = -2e_{31}V/\rho K_j$, $F(\omega_m, \omega_j) = 1/(\omega_m^2 - \omega_j^2)$. The first and the second summations on the right-hand side of equation (14) represent the vibrations induced by the driving signal ω_m and those contributed by the resonant modes, respectively. They are expressed by w_m and w_r , respectively. From equations (15a), (15b), we can find that the generation of traveling waves are determined by the bending angle $[\Phi'(x)]$ at edges of the two actuators at A_1 and A_2 . The difference of the bending angle between two edges determine the sign and magnitude of the four constants, A_j , B_j , C_j , and D_j . It provides a spatial controllable factor to control the generation of traveling waves, and it serves as the interface for optical manipulation of the OP-LM. Based on equation (14), the vibrations that can be used to induce a traveling wave are the waves generated by the driving frequency ω_m , and this can be decomposed as

$$w_m = [A_1\Phi_1(x) + A_2\Phi_2(x)]\sin(\omega_m t) + [B_1\Phi_1(x) + B_2\Phi_2(x)]\cos(\omega_m t). \quad (16)$$

From equation (16), we can find that traveling waves are generated by controlling the values of A_1 , A_2 , B_1 , and B_2 to be positive or negative. Table 1 summarizes the four possible combinations of these four constants to create traveling waves. The corresponding traveling directions of each condition are also listed. These four conditions make equation (16) to become two traveling waves propagated in the same direction. Otherwise, two propagating waves in opposite directions are induced. This analytical analysis shows that it is necessary to control the sign convention and magnitude of these four constants to generate traveling waves.

Figure 2 shows three different designs of the OP-LM. Mask 1 and mask 2 are symmetric, and mask 3 is a non-symmetric mask. The design of mask 3 can induce traveling

Table 1. Possible combinations of A_1 , A_2 , B_1 , and B_2 for generating a traveling wave on an OFTM piezoelectric linear motor.

A_1	A_2	B_1	B_2	Traveling direction
+	+	+	-	←
+	+	-	+	→
+	-	+	+	→
-	+	+	-	←

waves that propagate in opposite direction with respect to masks 1 and 2. Considering the profile of bending angle $\Phi'(x)$ of the first (blue line) and the second (red line) bending modes shown in figure 2, it was found that the first combination of A_1 , A_2 , B_1 , and B_2 in table 1 can be created by placing the two actuating areas symmetrically (mask 1 and mask 2). The locations of x_1 , x_2 , x_3 , and x_4 for mask 1 are chosen to be at $0.2L$, $0.4L$, $0.6L$, and $0.8L$ of a fixed-fixed OP-LM, respectively. The corresponding locations for mask 2 are $0.2L$, $0.486L$, $0.514L$, and $0.8L$. Thus, a configuration of $A_1 = B_1 > 0$, $A_2 = -B_2 > 0$, and $A_2 > A_1$ condition can be created and a traveling wave move to the negative direction (left) can be induced. Thus, equation (16) for mask 1 and mask 2 can be written as:

$$w_m = [A_1\Phi_1(x)\sin(\omega_m t) - A_2\Phi_2(x)\cos(\omega_m t)] + [A_2\Phi_2(x)\sin(\omega_m t) + A_1\Phi_1(x)\cos(\omega_m t)], \quad (17)$$

where both the first and the second term on the right-hand side represent propagating waves propagate to the negative direction (left). Furthermore, locations of x_1 and x_4 are designed to be near the anti-nodal points of $\Phi_1'(x)$ to have highest magnitude of A_1 and A_2 . The location of x_2 and x_3 for mask 2 was made closer to the nodal point of $\Phi_1'(x)$ to have a higher value of bending angle difference in equations (15a) and (15b) for mask 2. This design result in a lower amplitude of traveling waves, and mask 1 and mask 2 can be used to control the velocity of objects that the OP-LM carries.

On the other hand, the locations of x_1 , x_2 , x_3 , and x_4 for mask 3 were chosen to be $0.2L$, $0.4L$, $0.857L$ and L . This design results in $A_1, B_2, A_2 > 0$, $B_1 < 0$, and $B_2 > A_1$ and $A_2 > -B_1$ condition, which is the second case listed in table 1. Let $B_1 = -\beta_1$, and equation (16) becomes

$$w_m = [A_1\Phi_1(x)\sin(\omega_m t) + B_2\Phi_2(x)\cos(\omega_m t)] + [A_2\Phi_2(x)\sin(\omega_m t) - \beta_1\Phi_1(x)\cos(\omega_m t)]. \quad (18)$$

Having change of signs in the first and the second terms in equation (18), these two terms on the right-hand side represent two propagating waves move to the positive direction (right).

Figures 3(a) and (b) show simulated trajectories of peak amplitude of one complete cycle of generated traveling waves with respect to location and time using equations (17) and (18), respectively. Black lines and black dashed lines represent the traveling trajectories created by mask 1 and mask 2, respectively. Black arrow indicates its direction. The gray lines represents the traveling trajectories induced by mask 3, where its traveling direction is in opposite direction and is labeled with a gray arrow. The direction of generated

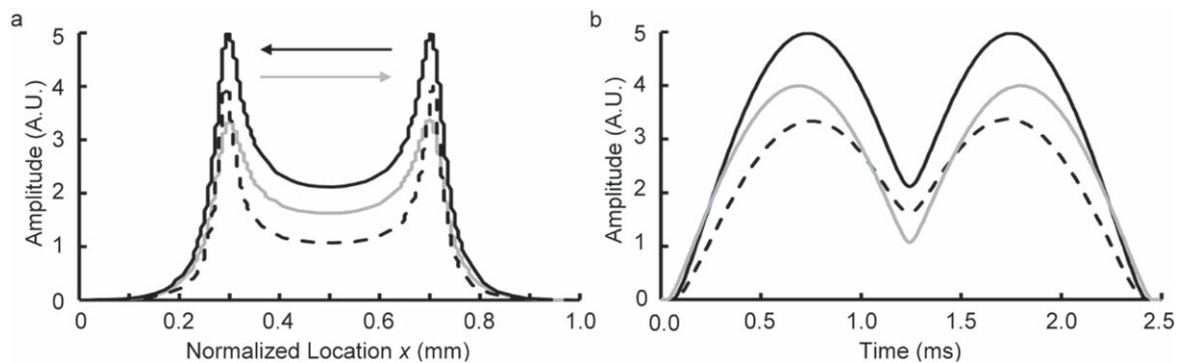


Figure 3. Trajectories of peak amplitudes of the simulated one cycle of generated traveling waves with respect to spatial location (a) and time (b), where black lines, black dotted lines, and gray lines represent trajectories of traveling waves generated by masks 1, 2, and 3, respectively.

traveling waves match theoretical predictions listed on table 1. The amplitude of the traveling wave generated by using mask 2 is also lower than mask 1 as predicted. The supplementary videos: S1.gif, S2.gif, and S3.gif is available online at stacks.iop.org/SMS/27/105050/mmedia show simulated traveling waves by using masks 1, 2 and 3, respectively. The capability to control traveling direction is clearly demonstrated.

3. Materials and experimental methods

3.1. Preparation of the TiOPc photoconductive coating solution

The TiOPc photoconductive coating precursor was prepared by dispersing Y-TiOPc (Sigma-Aldrich Co. LLC.) NPs in a polyvinyl butyral (PVB: Green Rich Technology Co., Ltd; P-90) resin dissolved in cyclohexanone (CYC) and methyl ethyl ketone (MEK) solvents. To enhance the electrical transport efficiency of the PVB resin, butadiene based hole transport material (HTM: Green Rich Technology Co., Ltd; C45) and quinone based electron transport material (ETM: Green Rich Technology Co., Ltd; P44) were blended into the solvent to promote the conductivity of the PVB resin. Furthermore, a high level of solid content of TiOPc NPs was used to reduce the electrical impedance of the photoconductive coating to match the electrical impedance of piezoelectric serial bimorph, where 30%, 40%, and 50% were used in this study. The surface tension (γ) of the precursor also was varied by adjusting the solvent ratio of CYC and MEK to study its contribution, as studies have shown that surface tension can play an important role on the structure formation of NPs in a coated film during the dip coating process [20]. The surface tension of CYC is 1.76 times higher than MEK, and three different CYC/MEK ratios were used, including 1/3 (low γ), 1/1 (medium γ), and 3/1 (high γ). They were labeled as C1M3, C1M1, and C3M1 in this paper, respectively. Table 2 summarizes all of the TiOPc photoconductive coating precursors and their corresponding labeling symbols used in this paper. The prepared precursor solution was applied onto one surface of a piezoelectric serial bimorph by the dip coating method. The speed of the dip coating process controlled the coating thickness to be within 1.6 and 5 μm . Finally, the

Table 2. Compositions and symbols of TiOPc photoconductive coating precursors studied in this paper.

Symbol	TiOPc solid content	CYC:MEK
[30%-C1M3]	30%	1:3
[30%-C1M1]	30%	1:1
[30%-C3M1]	30%	3:1
[40%-C1M3]	40%	1:3
[40%-C1M1]	40%	1:1
[40%-C3M1]	40%	3:1
[50%-C1M3]	50%	1:3
[50%-C1M1]	50%	1:1
[50%-C3M1]	50%	3:1

composition of each precursor was labeled as [TiOPc solid contents-solvent composition]. For example, [30%-C1M3] means a 30% solid content of TiOPc NPs with a 1–3 ratio of CYC and MEK solvent composition. ETM and HTM were added in all of the precursor solutions. To study the switching performance of electrical impedances before and after light activation of different coatings, each photoconductive coating was analyzed separately. They were first dip coated onto an indium-tin-oxide (ITO) sputtered glass slide followed by sputtering a 1 cm square 200 nm thick silver (Ag) electrode on its surface. The ITO bottom electrode served as a transparent electrode for optical access. The electrical impedance before and after light activation from 40 Hz to 5 kHz was measured by an impedance analyzer (Agilent 4294 A). A 3 W or a 10 W white-light power LED was used as the light source. Since TiOPc NPs were evenly distributed inside the PVB resin (figure 4(b)), the equivalent circuit of the photoconductive coating can be considered as multiple parallel-connected resistors and capacitances connected in series throughout the coating (figure 4(c)). It can further be simplified as a resultant resistor (R_{TiOPc}) and capacitance (C_{TiOPc}) connected in parallel (figure 4(c)). The overall frequency responses of the impedance Z_{TiOPc} were studied, and the optimal condition for matching the two actuating areas of the piezoelectric bimorph during on and off states was investigated.

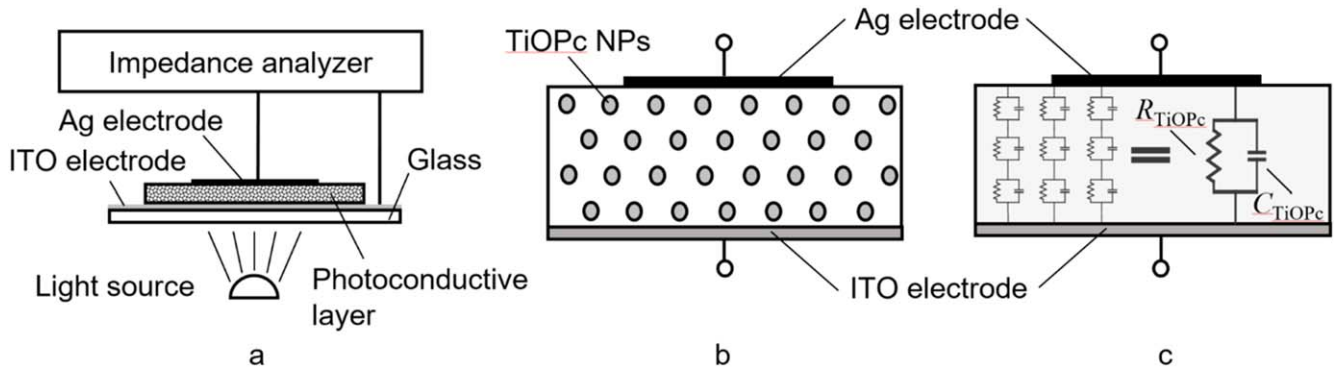


Figure 4. Illustrations of (a) the experimental setup for studying the performance of the photoconductive coating, (b) the distribution of TiOPc NPs in the photoconductive layer, and (c) the equivalent circuit.

3.2. Fabrication and experimental setup of the OP-LM

The configuration and experimental setup of the OP-LM are shown in figures 1(a) and (b). The OP-LM was fabricated using a commercial piezoelectric serial bimorph purchased from Eleceram Technology Co., LTD, where KA2-type and MD-type PZTs were used. The dimension of the fixed-fixed KA2-type OP-LM was 70 mm long by 5 mm wide by 0.4 mm thick, and it was used for the OP-LM study shown in figure 1(a). The dimension of fixed-fixed MD-type OP-LM was 60 mm long by 5 mm wide by 0.4 mm thick, and it was used for the design shown in figure 1(b). The thickness of each PZT sheet was 0.2 mm, and 200 nm thick Ag electrodes were coated on two external surfaces and between these two PZT sheets. The poling directions of PZT sheets were in opposite directions to form a serial bimorph. For the first design shown in figure 1(a), one side of the 200 nm thick silver surface electrode partially was removed, which left the areas from 14 mm (x_1) to 28 mm (x_2) and 42 mm (x_3) to 56 mm (x_4) intact to create the A_1 and A_2 surface electrodes. Then, the overall surface of this side was coated with a 2.2 μm thick TiOPc photoconductive coating followed by sputtering two 100 nm thick ITO transparent electrodes on the surface of these two actuating areas. The area of each ITO transparent electrode was 7 mm in length by 5 mm in width. This dimension of ITO electrodes was designed to control the working areas of TiOPc photoconductive coating for matching the electrical impedance of the piezoelectric serial bimorph at the two actuating areas (A_1 and A_2). They spanned between 21 mm to 28 mm and 42 mm to 49 mm on the 70 mm long OP-LM. Similar fabrication process was also conducted for the second design shown in figure 1(b), the difference is the Ag electrode was removed completely and two ITO electrodes were sputter-coated with a 1 mm separation at the center of the OP-LM.

To operate fabricated OP-LM, a multi-channel function generator (Good Will Instrument Co., Ltd, MGF-2260MFA) was used to generate two synchronized sinusoidal signals with a 90° phase difference. These two driving signals were amplified separately by two high-speed bipolar amplifiers (NF Corp., HSA 4052) to reach 160 V_{pp} . A 0.43 g aluminum nut, and stainless steel disks weighted in 0.2, 0.4, and 0.6 g were used as the object. They were placed at the center of an OP-

LM to monitor its performance. Two 10 W white light LEDs or LEDs with peak wavelength at 850 nm were used to activate the OP-LM. The performance of the OP-LM was investigated by studying the moving velocity of different objects, and the influence of light switching frequency on the transporting velocity.

3.3. Finite element analysis

The design of the OFTM OP-LM was verified by the finite element method. COMSOL® Multiphysics Simulator was used. A 3D model of a 70 mm long by 5 mm wide by 0.2 mm thick serial bimorph first was built in the software. Since the thickness of Ag electrodes, ITO electrodes, and TiOPc photoconductive electrodes were much thinner and softer than the PZT piezoelectric material, they were neglected in the finite element model. Piezoelectric constants of KA2 PZT provided by the vendor were input in the material parameter list. Piezoelectric strain coefficients were $d_{33} = 500 \text{ pC N}^{-1}$, $d_{31} = -210 \text{ pC N}^{-1}$, $d_{15} = 520 \text{ pC N}^{-1}$; elastic modulus were $E_{33} = 56 \text{ GPa}$ and $E_{11} = 65 \text{ GPa}$; relative dielectric constants were $\epsilon_{33} = 2000$ and $\epsilon_{11} = 1800$; and density was 7780 kg m^{-3} . Two areas of the top surface were designed to be the top surface electrodes A_1 and A_2 , and their location and size were set according to the three designs shown in figure 2. The bottom electrode of the LM was grounded. Two ends of the LM boundaries were both fixed. The eigenvalue problem was conducted first to find resonant frequencies of the first three bending modes. Then, a frequency between the first and the second bending modes was chosen and assigned as the driving frequency ω_m of the two top electrodes. The driving voltages of the first and the second top electrodes were set to be $160 \cdot \sin(\omega_m t)$ and $160 \cdot \cos(\omega_m t)$ volts, respectively. Finally, a time-dependent study was used to simulate the vibration pattern of traveling waves induced by the OFTM driving method with three different mask designs.

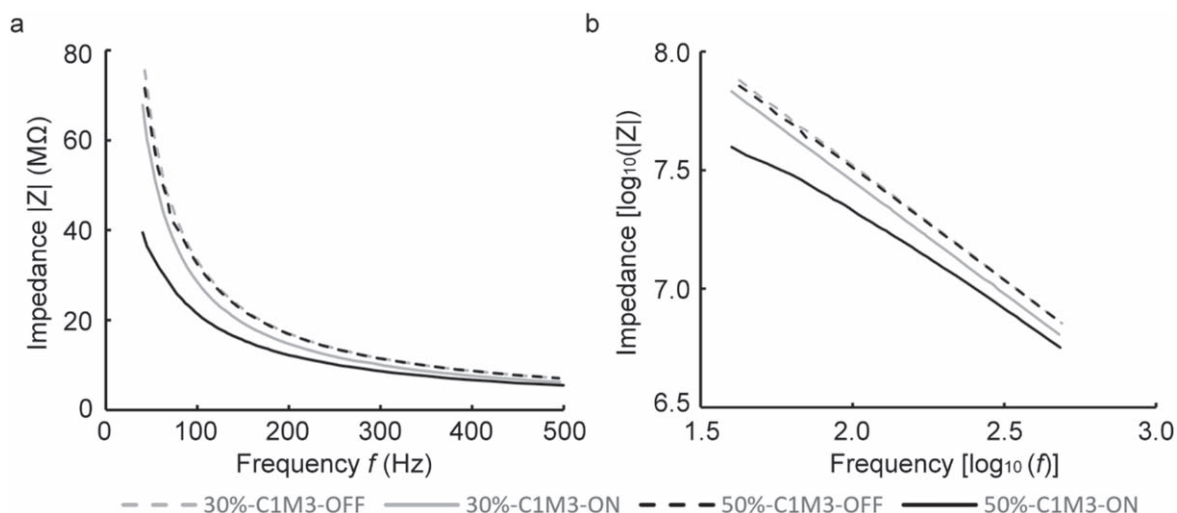


Figure 5. Impedance responses of two TiOPc photoconductive coatings under conditions of [30%-C1M3] (gray lines) and [50%-C1M3] (black lines), where the corresponding thicknesses are 1.96 and 1.62 μm . The dashed and solid lines represent impedance under light-off and light-on conditions, respectively.

4. Results

4.1. Impedance response of the TiOPc photoconductive coating

To study the impedance response of the TiOPc photoconductive coating with different compositions, the frequency response of each coating was measured and analyzed. Figures 5(a) and (b) show an example of measured impedance response in linear and log–log scale, respectively. The activating light source was a 3 W white light LED. The dashed and solid gray lines are responses of the [30%-C1M3] condition under light-off and light-on states, respectively. On the other hand, the dashed and solid black lines are the ones of [50%-C1M3] conditions under light-off and light-on conditions, respectively. The phase responses were around -90° for all conditions throughout 40 Hz to 5 kHz study range. This result showed that the characteristic impedance of TiOPc coating was dominated by the capacitance response with a large resistance for both light-off and light-on states. This set of data also demonstrated that both coating conditions had a higher on–off ratio at lower frequency range and decreased at higher frequency. It also suggests that the coatings with a higher TiOPc composition can have a much better on–off ratio and lower range of electrical impedance. These characteristics held for all three different solvent compositions listed in table 2 (summarized in figure 6). This finding suggested that a better on–off ratio could be achieved using a higher weight percentage of TiOPc NPs and operating the photoconductive coating at a lower frequency range. Furthermore, the level of electrical impedance could be lowered by increasing the weight-percentage of TiOPc NPs. This demonstrated that the electrical impedance could be adjusted by controlling the TiOPc concentration. Note also that, after converting to a log–log plot (figure 5(b)), the impedance response could be fitted by a linear equation $y = ax + b$,

where a and b are correlated to the capacitance and resistance behaviors of each coating.

Since different thicknesses were studied, we first divided impedance response with measured film thickness and compared fitted a and b values. Both light-off (a_{OFF} and b_{OFF}) and light-on (a_{ON} and b_{ON}) states were studied and are shown in figures 6(a)–(d). The data of nine different coating conditions (table 2) studied in this research were labeled by the following methods. First, the ratios of CYC and MEK were labeled as blue, red, and green for C1M1, C1M3, and C3M1, respectively. Second, the 30%, 40%, and 50% weight percentages of TiOPc NPs were labeled with triangles, diamonds, and circles, respectively. From the measured a_{OFF} and a_{ON} shown in figures 6(a) and (b), one can see that the fitted slope a is all in negative values and decreases along with a higher thickness for both light-off and light-on states. This suggests that the contribution of capacitance decreases with higher coating thickness. Similar behaviors are also found for both b_{OFF} and b_{ON} , shown in figures 6(c) and (d). Furthermore, the fitted a and b for all nine conditions fall into the same curve, suggesting that thickness is a dominating factor. Finally, to study the performance of on–off ratio ($Z_{\text{OFF}}/Z_{\text{ON}}$), the difference $\Delta a = a_{\text{ON}} - a_{\text{OFF}}$ and $\Delta b = b_{\text{ON}} - b_{\text{OFF}}$ is compared and shown in figures 6(e) and (f), respectively. This analysis shows that thinner coatings have a higher Δa and Δb for both 40% and 50% TiOPc conditions but not for the 30% condition in general. Furthermore, a high concentration of TiOPc NPs with 50% weight percentage can have a higher impedance change, and the condition of [50%-C1M3] has the highest Δa and Δb values. This result suggests that [50%-C1M3] can provide the highest on–off ratio among all of coating conditions.

4.2. Contribution of light intensity to on–off ratio

Since the performance of 50% TiOPc photoconductive coatings can provide a larger on–off ratio and lower impedance

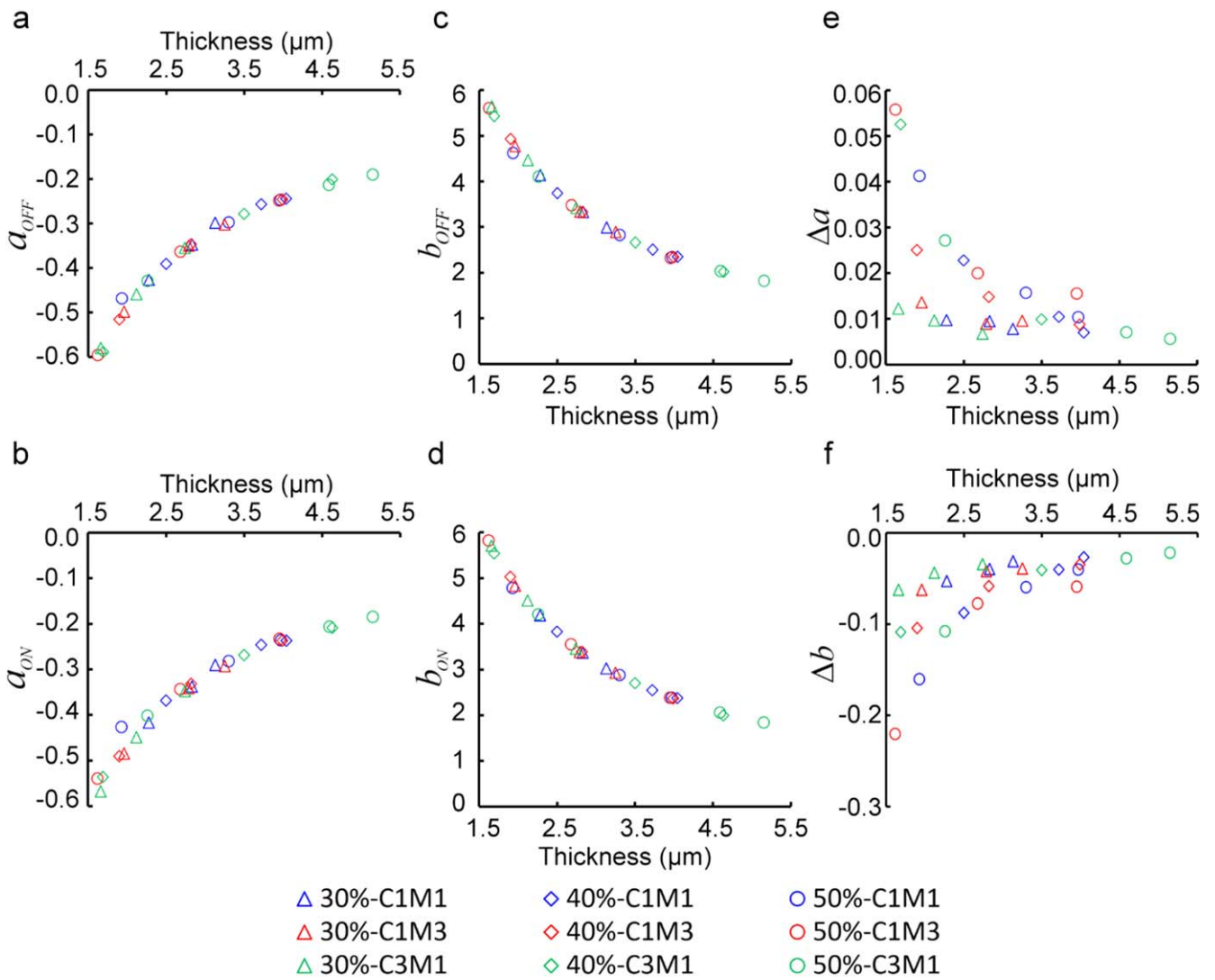


Figure 6. Curve-fitted values of a and b of the linear asymptote line ($y = ax + b$) with respect to the impedance response in log–log scale during light-off (a), (c), (e) and light-on (b), (d), (f) conditions, where (a) and (b) are the slope a , (c) and (d) are y value b when $x = 0$, (e) is the difference between a ($a_{ON} - a_{OFF}$), and (f) is the difference between b ($b_{ON} - b_{OFF}$).

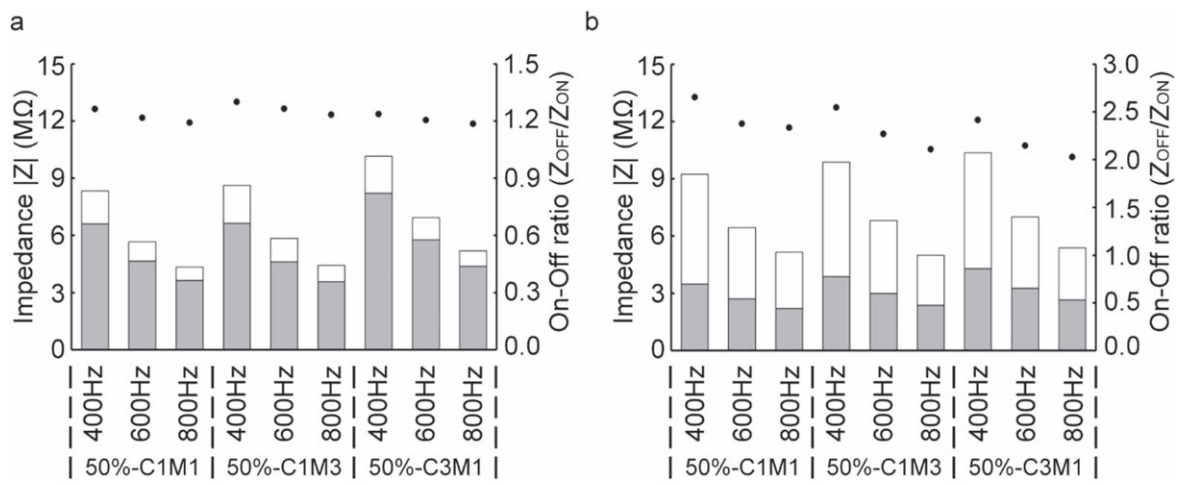


Figure 7. Measured impedance values (left y-axis) during light-off (white bars) and light-on (gray bars) conditions under (a) 3 W and (b) 10 W light intensities. The black dots are corresponding on–off ratios (right y-axis).

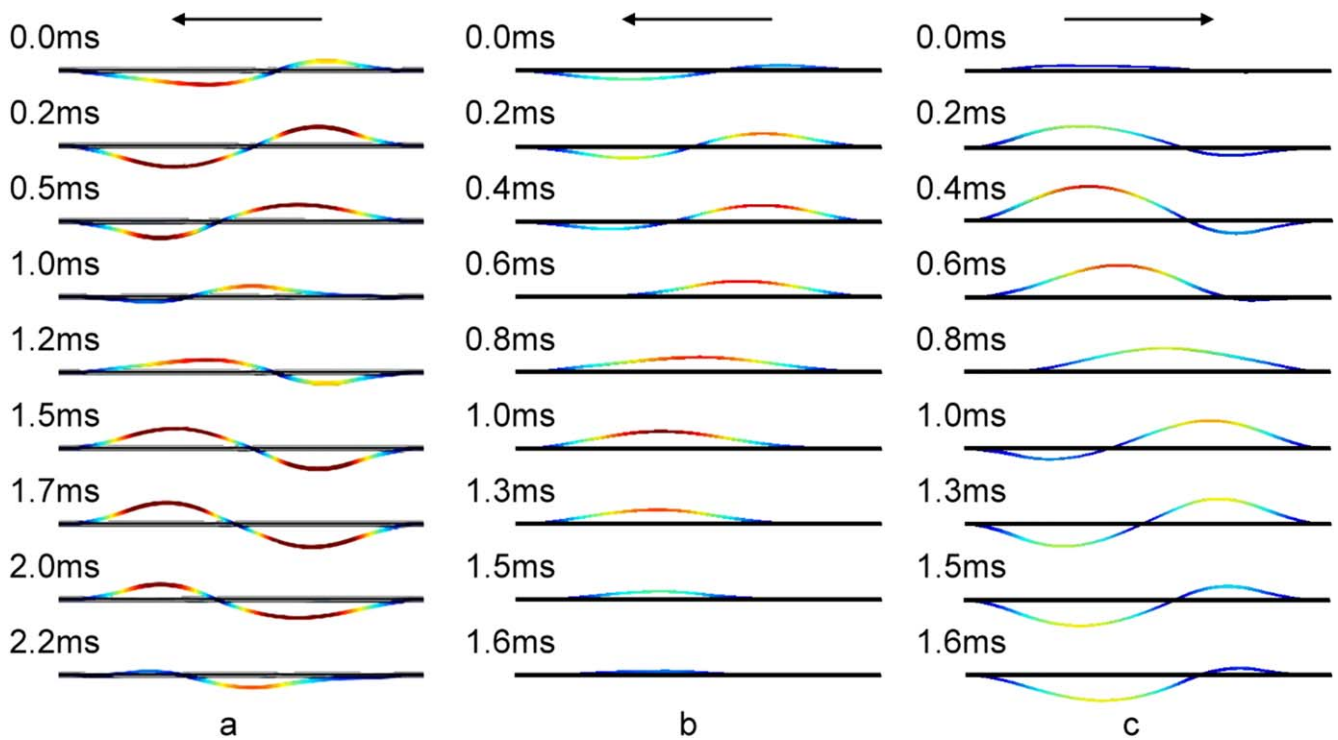


Figure 8. Time-lapse images of simulated traveling waves generated via OFTM method by using mask 1 (a), mask 2 (b) and mask 3 (c).

range, we used [50%-C1M1], [50%-C1M3], and [50%-C3M1] coatings to study the contribution of light intensity. Two levels of light intensity were studied, 3 W and 10 W white-light LEDs. Figures 7(a) and (b) show measured on–off ratio for these three compositions at 400 Hz, 600 Hz, and 800 Hz with respect to 3 W and 10 W light energy, respectively. White and gray bars are the corresponding impedance values at light-off and light-on states. The black dots represent the corresponding on–off ratio (Z_{OFF}/Z_{ON}). This experimental result shows that the on–off ratio decreases at higher frequency and a higher on–off ratio can be achieved under a higher light intensity. Under a high light intensity of 10 W and operated at 400 Hz, the on–off ratio of [50%-C1M1], [50%-C1M3], and [50%-C3M1] are 2.65, 2.54, and 2.42, respectively. The corresponding averaged increment of on–off ratio from an increase of 3.33 times light energy was 2.01, 1.82, and 1.82 fold with standard deviations of 0.08, 0.13, and 0.13. This result suggests that the surface tension of coating precursor needs to be low to increase switching performance, where [50%-C1M1] and [50%-C1M3] offers better performance than [50%-C3M1]. Based on the experimental findings, the composition of [50%-C1M3] was chosen as the photoconductive coating in the following experiments for matching the electrical impedance of the piezoelectric serial bimorph.

4.3. Finite element analysis

The simulation results showed that the resonant frequencies of the first three bending modes of the 70 mm long KA2-type OP-LM were 265.7 Hz, 660.8 Hz, and 1317.5 Hz, respectively. Knowing that the on–off ratio of the photoconductive

coating was highest at 400 Hz in figure 7, the driving frequency ω_m of the OFTM was set at 400 Hz. The driving voltage for the left (A_1) and the right (A_2) actuating areas were $160 \cdot \sin(\omega_m t)$ and $160 \cdot \cos(\omega_m t)$ volts, respectively. Figures 8(a)–(c) show time-lapse images of the simulated time-dependent results for one complete cycle of generated traveling waves by using masks 1, 2 and 3, respectively. The simulation result verified that using masks 1 and 2 can control the sign convention of four constants shown in equation (17), and traveling waves can be generated and moved from right to left. The supplementary videos S4.gif and S5.gif show corresponding animations of simulated traveling waves. They have similar vibrating patterns and have identical moving direction as the theoretical prediction shown in figure 3. Furthermore, the simulation results of mask 1 and 2 demonstrated that the OP-LM with mask 2 had a lower amplitude than the one with mask 1. It can be used to control the moving velocity of object been carried. On the other hand, the traveling wave that propagated toward the opposite direction was also simulated by using mask 3 (figure 8(c)). Its animated movie is provided in supplementary video S6.gif. Note that there were three different levels of propagating waves, and they all propagated from left to right. This effect could due to the design was not symmetric, and the two propagating waves in equation (18) were not in phase. This experimental result verified that using the design of mask 3, the sign convention of the four constants shown in equation (18) also can be spatially controlled. In summary, simulation results verified the theoretical analysis and demonstrated the feasibility of frequency selection of ω_m and the design of three different types of masks.

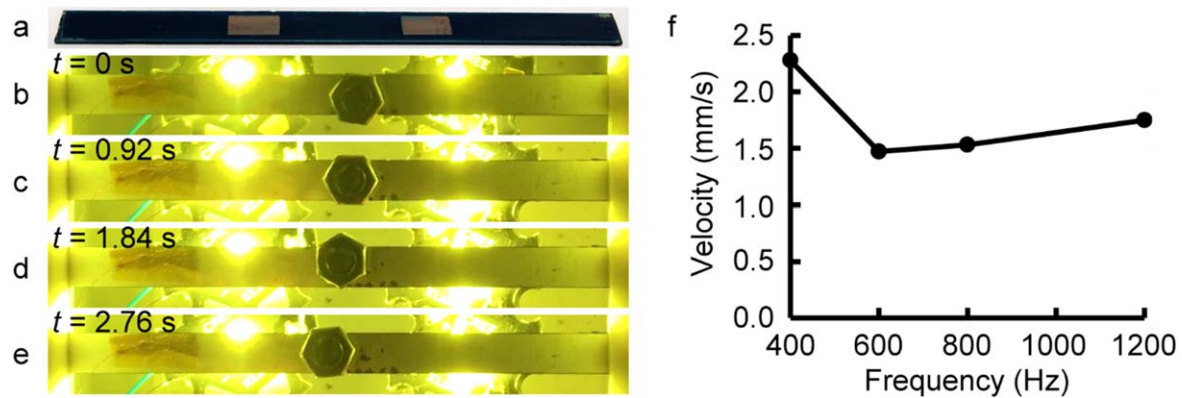


Figure 9. (a) An image of fabricated optopiezoelectric liner motor, and (b)–(e) time-lapse images of an object moved by the OP-LM at 400 Hz driving frequency and 400 Hz light switching frequency. (f) is the measured moving velocity of the object driven by the OP-LM under different light switching frequencies.

4.4. Experimental results of the OP-LM

The resonant frequencies of the first two bending modes of the piezoelectric serial bimorph first were measured by an impedance analyzer before applying the TiOPc photoconductive coating, where A_1 and A_2 actuating Ag electrodes were already released. The measured resonant frequencies of 70 mm long KA2-type OP-LM were at 235.6 Hz and 737.2 Hz, respectively. The OFTM driving frequency also was chosen to be 400 Hz to have a good on–off ratio and impedance range, as suggested in figure 7. This frequency was between the resonant frequencies of the first and the second bending modes. Using A_1 and A_2 electrodes of mask 1 (figure 2), the combination of the first sign convention suggested in table 1 and equation (17) can be created. The measured electrical impedance of the piezoelectric serial bimorph at 400 Hz was 1.01 M Ω . To match the impedance of the piezoelectric serial bimorph, a 2.2 μm thick [50%-C1M3] photoconductive coating was applied on the surface of the piezoelectric linear motor. Furthermore, the area of the top ITO transparent electrodes were designed to be half (7 mm by 5 mm) of the two A_1 and A_2 Ag electrodes (14 mm by 5 mm) to control the working area of the coating and to match the electrical impedance of the piezoelectric linear motor. This provided 5.46 and 2.13 M Ω electrical impedance during light-off and light-on states using a 10 W white-light LED. This design can provide a 24.8 V_{pp} (15.5%) and 51.1 V_{pp} (32.1%) driving voltage across the piezoelectric serial bimorph during light-off and light-on states, respectively. A 0.43 g aluminum nut was used as the object to verify OP-LM performance. The experimental procedure was first to apply a 400 Hz 160 V_{pp} driving source to the OP-LM for a few seconds followed by activating it with a switching light source. The direction and trajectory of the aluminum nut on the OP-LM was monitored. Experimental results showed that, under a light-off condition, the OP-LM could not move the 0.43 g aluminum nut, suggesting that a 24.8 V_{pp} driving voltage across the piezoelectric serial bimorph was insufficient to push it. After lowering the impedance of the photoconductive coating with light activation and increasing the driving voltage across the piezoelectric serial bimorph to 51.1 V_{pp} , the aluminum nut was

moved on the surface of the OP-LM. This result suggests that the TiOPc photoconductive coating can provide sufficient switching performance to control the movement of an object on the OP-LM.

Figure 9(a) shows an image of fabricated KA2-type OP-LM, where the dark blue area and silver rectangles are the TiOPc photoconductive coating and ITO transparent electrodes, respectively. Figures 9(b)–(e) show time-lapse images of the aluminum nut moved by the OP-LM under a 10 W light activation for each actuator. The moving velocity was 2.28 mm s^{-1} under a 400 Hz light switching frequency. Note that the moving direction was also from the right to left, which matched well with analytical analysis (figure 3: black lines) and simulation results (figure 8(a)). We further studied the contribution of light switching frequency to the moving velocity. The switching frequency was increased from 400 Hz to 1.2 kHz. The experimental finding showed that the moving velocity started to decrease at higher frequency range but increased a bit at 800 Hz and 1.2 kHz, as shown in figure 9(f). This result matched the experimental findings in our previous work in optopiezoelectric micropumps [9], where an optimal condition could be achieved using identical frequencies for both light source and driving signal. Thus, the light induced electron–hole pairs could be thoroughly used during each cycle, where excess electrons and holes could be depleted during the light-off state. Thus, electrons or holes would not be trapped inside the TiOPc NPs and eventually cease the operation. We also found that the moving velocity reduced 36% at 600 Hz switching light source. Nevertheless, it became only 33% and 23% reduction of moving velocity at 800 Hz and 1.2 kHz switching frequency, which were both integral multiples of 400 Hz. These results suggested that matching the switching frequency between light source and driving voltage was important for using a TiOPc photoconductive coating to act as an optical interface for an activate component like a piezoelectric liner motor. Finally, the supplementary video S7.wmv is the experimental result shown in figures 9(a)–(e). It shows that the object cannot be moved during the light-off state, even when the driving source was applied. It started to be moved once the light source was switched on and stopped again after the light was turned off.

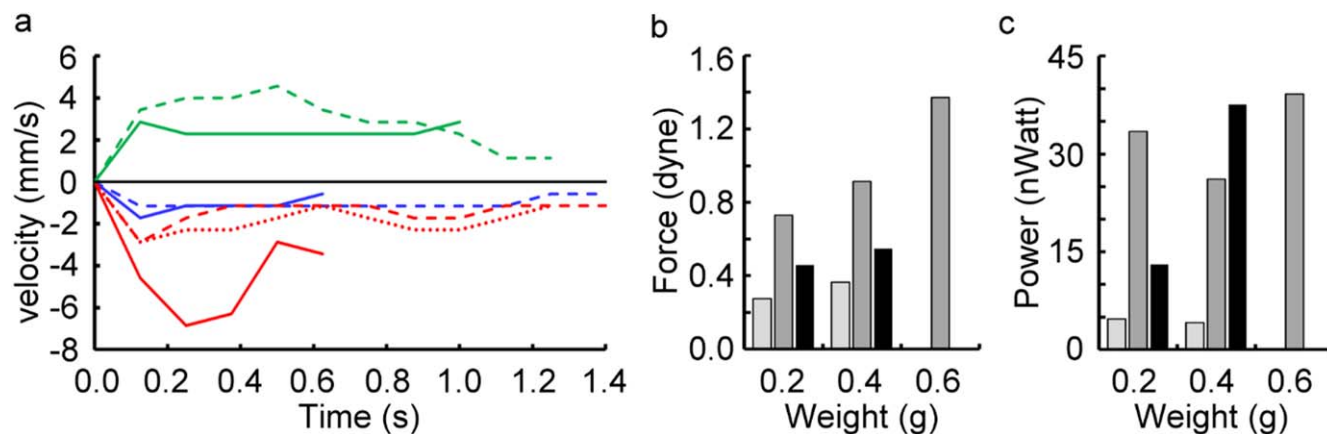


Figure 10. (a) Measured moving velocity of 0.2 g (solid lines), 0.4 g (dashed lines), and 0.6 g (dotted lines) objects driven by OP-LMs activated with mask 1 (blue lines), mask 2 (red lines), and mask 3 (green lines). (b) and (c) are the estimated driving force and power for initiating object movement, where light gray, dark gray, and black bars represent mask 1, 2 and 3 results.

To verify the concept of the OP-LM and to study its performance, the 60 mm long MD-type OP-LM and the design shown in figure 1(b) was used. The 10 W 850 nm LED light source was used for this study, and the performance of three mask designs shown in figure 2 were compared. The measured resonant frequencies of the first and the second bending modes were 251.2 kHz and 698.9 kHz, respectively. The OFTM driving frequency was also chosen at 400 Hz, and a 160 V_{pp} driving voltage was applied. Since the actuating area was determined by a mask, the impedance match was based on the thickness of the piezoelectric bimorph and the photoconductive coating. The measured percentages of the voltage that delivered to the piezoelectric bimorph were 17.0% (27.3 V_{pp}) and 25.6% (41.0 V_{pp}) during light-off and light-on states, respectively. Using this setup, we study the velocity of 0.2, 0.4 and 0.6 g objects moved by the OP-LM. Objects weighted higher than 0.8 g was not able to be moved by current OP-LM configurations. Figure 10(a) shows measured velocity fluctuations over time. Solid, dashed and dotted lines represent measured velocities of 0.2 g, 0.4 g and 0.6 g objects, respectively. Blue, red and green lines are results of objects been moved by using masks 1, 2 and 3, respectively. Note that the velocity of objects moved by using masks 1 and 2 were negative. This was because they were pushed toward negative direction as designed. This result also demonstrated that the moving velocity can be altered by changing the activating areas between masks 1 and 2. On the other hand, the measured velocities of objects driven by OP-LM activated with mask 3 were positive as designed. The supplementary video S8.wmv shows one of the video recordings of this design, where the weight of the object was 0.4 g. Note that the light source was not visible since its peak wavelength was 850 nm. Finally, these experimental results demonstrated that the moving velocity can be relatively stable for a certain object in each mask design. This effect could be due to the amplitudes and profiles of traveling waves were different as shown in figure 3(a). A light weight object could bounce a lot on the OP-LM during movement and cause velocity fluctuations. It was found that only OP-LM activated by mask 2 can move 0.6 g object. Figures 10(b) and (c) shows

estimated driving force and power to initiate object movement by using different masks. The driving force was in dyne range, and it was higher with a heavier object. The driving power was in several tens of nano-Watts, and it was much lower for OP-LM activated with mask 1. This result could be due to the amplitude of traveling wave induced by mask 1 was higher than the other two masks, and it made objects bounce on the OP-LM instead of moving forward.

5. Discussions

Using a piezoelectric bimorph to serve as the core of the piezoelectric linear motor offers a number of advantages over previous reported motors. First, its structure is simple since it does not need a complex arrangement of multiple piezoelectric actuators on the motor structure. Second, its fabrication process is well-developed and more cost effective than piezoelectric stacks. Third, its operation principle is simple and straightforward. However, the performance of the OP-LM is lower than most of reported piezoelectric motors based on frequency leveraged method. A comprehensive review can be found in a recent paper reported by Peng *et al* [21]. They separated this type of piezoelectric motors into three major categories, including ultrasonic motors, quasi-static motors, and hybrid motors of previous two methods. The developed methods for ultrasonic motors can further be divided into two categories: standing wave type and traveling wave type. The present method belongs to the traveling wave type motor. The velocity range of standing wave type motors is above several hundred rpm and mm s^{-1} with output torque ranging from tens of nNm to several hundreds of mNm. On the other hand, the velocity range of quasi-static motors is slower, it ranges from sub- mm s^{-1} to tens of mm s^{-1} with a couple examples can go over one hundred mm s^{-1} . Its output power is in the range of tens of milli-Newtons to tens of Newtons. As for the traveling wave type motors like a surface acoustic wave motor and Sashida motor [21, 22], the transfer speed can reach 200 mm s^{-1} and tens of rpm, respectively. For the piezoelectric motors driven by two-mode excitation, the

velocity ranges from sub-cm s⁻¹ to tens of cm s⁻¹ with a sub-mNm torque output [10–12, 15]. The output performance of the OP-LM in this configuration is lower than these reported motors. Nevertheless, we clearly demonstrated that using the developed optopiezoelectric composite to serve as the core structure of a linear motor, the direction and velocity of carried object can be controlled optically.

To improve OP-LM, the performance of the TiOPc photoconductive coating should further be optimized to enhance the motor performance by increasing the voltage applied on the piezoelectric bimorph. One potential solution is to match the illuminating spectrum of the light source with the absorption spectrum of TiOPc NPs. The switching performance of the electrical impedance could increase significantly. Furthermore, the operating bandwidth of the TiOPc photoconductive coating also should be improved further for higher frequency range, and the moving velocity of carried objects can be increased by using higher resonant modes. Thus, the advantage of frequency leverage method can be applied. Furthermore, the thickness of the piezoelectric bimorph versus object/slider weight should also be optimized to increase output power. Finally, the surface of the OP-LM also can be modified to enhance output performance and to minimize objects bouncing on its surface.

6. Conclusion

In this paper, a light-activated piezoelectric linear motor named OP-LM is reported. This OP-LM was constructed by a ceramic-based optopiezoelectric composite composed of a piezoelectric serial bimorph and an ITO sputtered TiOPc photoconductive coating. In order to match the electrical impedance of the piezoelectric serial bimorph in MΩ range, the electrical impedance of standard TiOPc coatings needs to be significantly reduced. To achieve this goal, we conducted a series of study on the composition of the TiOPc photoconductive coating precursors. Parameters included the solid content of TiOPc NPs, thickness, and solvent compositions. Furthermore, ETM and HTM were dispersed in the PVB resin to enhance its conductivity. It was found that, using a high concentration of TiOPc NPs with ETM and HTM embedded PVB resin, the electrical impedance of TiOPc photoconductive material could be significantly reduced. It also was found that a good on–off ratio could be created using a 50% TiOPc coating and a thin coating thickness. The on–off ratio, however, decreased along with higher frequencies. We also found that the impedance level was influenced by the solvent compositions, where solvents with lower surface tension can result in a lower impedance values. Finally, we demonstrated that the on–off ratio and electrical impedance could reduce further with a higher light intensity. Based on the study of TiOPc coatings, we successfully used the [50%-C1M3] photoconductive coating to match the electrical impedance of the piezoelectric serial bimorph. The voltage applied on the bimorph could be switched optically between 24.8 V_{pp} and 51.1 V_{pp} for KA2-type OP-LM and be switched optically between 27.3 V_{pp} and 41.0 V_{pp} for MD-type OP-LM. We

demonstrated that this combination was sufficient to control the movement of an object placed on the surface of the OP-LM optically. A moving velocity in the range of tens of several mm/s was achieved. Furthermore, it was found that the optimal light switching frequency was to match the driving frequency of the OP-LM, and the moving direction can be controlled optically.

To design the OP-LM to be driven by the OFTM method, we derived an analytical solution to describe the driving mechanism. Based on the developed general solution, we concluded that the main factor to generate a traveling wave using a single frequency between two adjacent bending modes was the sign convention of the four constants in equation (16). By controlling the location and size of the two actuating areas, we can control the sign and value of these four constants, along with the direction of induced traveling waves. Applying this theory, three different masks were designed. Finite element simulation was used to verify these designs, and identical moving direction of traveling waves was evident. These designs also were experimentally studied, and the moving direction of generated traveling waves matched the prediction of the analytical analysis and can be optically controlled. Finally, the derived analytical solution also can be applied to design linear motors at high resonant modes. Lastly, the concept of OP-LM can further scale up to linear motor array or 2D motor to introduce dynamic optical control.

Acknowledgments

This work is supported by the Ministry of Science and Technology, ROC [MOST 103-2627-E-002-004-].

ORCID iDs

Yu-Hsiang Hsu  <https://orcid.org/0000-0002-9759-7848>

Reference

- [1] Neale S L, Mazilu M, Wilson J I, Dholakia K and Krauss T F 2007 The resolution of optical traps created by light induced dielectrophoresis (LIDEP) *Opt. Express* **15** 12619
- [2] Chiou P Y, Ohta A T and Wu M C 2005 Massively parallel manipulation of single cells and microparticles using optical images *Nature* **436** 370
- [3] Huang S B, Liu S L, Li J T and Wu M H 2014 Label-free live and dead cell separation method a using high-efficiency optically induced dielectrophoretic (ODEP) force-based microfluidic platform *Int. J. Autom. Smart Technol.* **4** 83
- [4] Shah G J, Ohta A T, Chiou E P, Wu M C and Kim C J 2009 EWOD-driven droplet microfluidic device integrated with optoelectronic tweezers as an automated platform for cellular isolation and analysis *Lab Chip* **9** 1732
- [5] Yang S M, Yu T M, Huang H P, Ku M Y, Hsu L and Liu C H 2010 Dynamic manipulation and patterning of microparticles and cells by using TiOPc-based optoelectronic dielectrophoresis *Opt. Lett.* **35** 1959

- [6] Yang S M, Yu T M, Huang H P, Ku M Y, Tseng S Y, Tsai C L, Chen H P, Hsu L and Liu C H 2011 Light-driven manipulation of picobubbles on a titanium oxide phthalocyanine-based optoelectronic chip *Appl. Phys. Lett.* **98** 153512
- [7] Yu T M, Yang S M, Fu C Y, Liu M H, Hsu L, Chang H Y and Liu C H 2013 Integration of organic opto-electrowetting and poly(ethylene) glycol diacrylate (PEGDA) microfluidics for droplets manipulation *Sensors Actuators B* **180** 35
- [8] Jiang D and Park S Y 2016 Light-driven 3D droplet manipulation on flexible optoelectrowetting devices fabricated by a simple spin-coating method *Lab Chip* **16** 1831
- [9] Wang H H, Wu T J, Lin S J, Gu J T, Lee C K, Cheng I C and Hsu Y H 2017 Dual light-activated microfluidic pumps based on an optopiezoelectric composite *J. Micromech. Microeng.* **27** 125003
- [10] Kuribayashi M, Ueha S and Mori E 1985 Excitation conditions of flexural traveling waves for a reversible ultrasonic linear motor *J. Acoust. Soc. Am.* **77** 1431
- [11] Takano T and Tomikawa Y 1989 Linearly moving ultrasonic motor using a multi-mode vibrator *Japan. J. Appl. Phys.* **28** 164
- [12] Tomikawa Y, Adachi K, Hirata H, Suzuki T and Takano T 1990 Excitation of progressive wave in a flexurally vibrating transmission medium *Proc. 10th Symp. Ultrason. Electron.* vol 29, p 179
- [13] Hariri H, Bernard Y and Razek A 2014 A traveling wave piezoelectric beam robot *Smart Mater. Struct.* **23** 025013
- [14] Hariri H, Bernard Y and Razek A 2015 Dual piezoelectric beam robot: the effect of piezoelectric patches' positions *J. Intell. Mat. Syst. Struct.* **26** 2577
- [15] Loh B and Ro P I 2000 An object transport system using flexural ultrasonic progressive waves generated by two-mode excitation *IEEE Trans. Ultrason. Ferroelectr. Freq. Control* **47** 994
- [16] Dehez B, Vloebergh C and Labrique F 2010 Study and optimization of traveling wave generation in finite-length beams *Math. Comput. Simulat.* **81** 290
- [17] Chen T H, Wang H H, Hsu Y H and Lee C K 2016 Integrating optopiezoelectric actuators and a two-mode excited linear ultrasonic motor for microfluidics *Proc. SPIE* **9705** 97050Q
- [18] Lee C K 1992 Piezoelectric laminates: theory and experiments for distributed sensors and actuators *Intelligent Structural Systems* ed H S Tzou and G L Anderson (Dordrecht: Kluwer) pp 75–167
- [19] Lee C K 1990 Theory of laminated piezoelectric plates for the design of distributed sensors/actuators: I. Governing equations and reciprocal relationships *J. Acoust. Soc. Am.* **87** 1144
- [20] Cong H and Cao W 2003 Colloidal crystallization induced by capillary force *Langmuir* **19** 8177
- [21] Peng Y, Peng Y, Gu X, Wang J and Yu H 2015 A review of long range piezoelectric motors using frequency leveraged method *Sensors Actuators A* **235** 240
- [22] Uchino K 1998 Piezoelectric ultrasonic motors: overview *Smart Mater. Struct.* **7** 273